Retrieval of large-scale wind divergences from infrared Meteosat-5 brightness temperatures over the Indian Ocean

M. Bonazzola, L. Picon, H. Laurent, F. Hourdin, G. Seze, H. Pawlowska, R. Sadourny

JOURNAL OF GEOPHYSICAL RESEARCH, VOL. 106, NO. D22, PAGES 28,113–28,128, NOVEMBER 27, 2001

Retrieval of large-scale wind divergences from infrared Meteosat-5 brightness temperatures over the Indian Ocean

M. Bonazzola,[1] L. Picon,[1] H. Laurent,[2] F. Hourdin,[1] G. Sèze,[1]
H. Pawlowska,[3] and R. Sadourny[1]

Abstract. Over the tropics the atmospheric general circulation models usually fail in predicting horizontal wind divergence, which is closely related to atmospheric heating and to the vertical exchanges associated with convection. With the aim of forcing atmospheric models we present here a reconstruction of wind divergences based on the links between infrared brightness temperatures, convective activity, and large-scale divergence. In practice, wind divergences are reconstructed from brightness temperatures using correlations obtained from numerical simulations performed with a general circulation model. When building those correlations, a distinction must be made between the brightness temperatures of opaque clouds and those of semitransparent clouds, only the former being directly associated with convection. In order to filter out semitransparent clouds we use radiative thresholds in the water vapor channel in addition to the window channel. We apply our approach to Meteosat-5 data over the Indian Ocean. Comparison with wind divergences reconstructed independently from Meteosat water vapor winds partially validates our retrieval. Comparison with European Center for Medium-Range Weather Forecasts analyses indicates that much can be gained by adding information on the wind divergence in the tropics to force an atmospheric model.

1. Introduction

The retrieval of global wind fields constitutes a challenging and essential task for analysis and numerical weather prediction. Direct wind observations are indispensible at low latitudes, where winds cannot be accurately inferred from the mass field. The global network of geostationary satellites provides the basis for the derivation of cloud motion winds from successive aligned satellite images. Until recently, the Indian Ocean was poorly observed because of the difficulty of accessing INSAT data. The situation changed in June 1998, when the European Organization for the Exploitation of Meteorological Satellites (EUMETSAT) shifted Meteosat-5 to 63°E, on request of scientists involved in the Indian Ocean Experiment (INDOEX). This allowed the derivation of cloud motion winds from the infrared window channel (10.1-13.1 μm, labelled IR), from the water vapor band (5.5-7.3 μm, labelled WV), and from the visible channel (0.3-1.04 μm, labelled VIS) over this area. This new information has been routinely assimilated at the European Center for Medium-Range Weather Forecasts (ECMWF) since August 12, 1998.

An accurate estimation of wind divergence is particularly important in the tropics, since this quantity is closely related to the vertical exchanges associated with convection. *Laurent and Sakamoto* [1998] have studied the feasibility of estimating the upper level wind divergence associated with tropical convective cloud systems from water vapor winds. However, the retrieval of wind divergence from wind estimates is very sensitive to small-scale noise or errors getting amplified by finite differencing. In addition, the retrieval is restricted to a small number of layers (near the surface, at cloud drift levels, or at the WV weighting function peak level) that are only approximately located, because of the difficulty of determining precisely the altitudes of clouds and WV structures.

We present here an alternative approach, where wind divergences are retrieved from infrared Meteosat-5 brightness temperatures. Our retrieval is performed in two steps. First an atmospheric general circulation model (AGCM) is used in a climatic mode to define statistical relations between model wind divergences at different levels and synthetic IR brightness temperatures defined

[1]Laboratoire de Météorologie Dynamique du CNRS, Paris, France.
[2]Laboratoire d'étude des Transferts en Hydrologie et Environnement de l'Institut de Recherche pour le Développement, Paris, France.
[3]Institute of Geophysics, University of Warsaw, Warsaw, Poland

Paper number 2000JD900690.
0148-0227/01/2000JD900690$09.00

in the channels of Meteosat. In a second step we then apply the statistical relations to the geostationary images of the brightness temperatures to retrieve the divergence field.

This approach has definite interests from several viewpoints. First, the method uses information that is not fully contained in the EUMETSAT wind products; therefore it can be used to improve the divergent circulation and diabatic heating field in numerical initializations. Furthermore, it provides statistical information on the whole vertical profile of wind divergence. The quantitative magnitudes of the divergences cannot really be retrieved, because of the large error bars associated with our estimates and, further, because they depend on model characteristics, especially the parametrization of convection and biases in thermal stratification and water vapor transport. However, these divergence profiles are appropriate to nudge the initial state toward the inclusion of better located convective systems, while keeping consistency with the AGCM dynamics. This approach is related to what has been refered to as "physical initialization" methods in data assimilation [e.g., *Krishnamurti et al.*, 1991]. An alternative way to nudge the initial state to a better retrieval of convective activity is to use rainfall data including space observations like those of Special Sensor Microwave Imager (SSM/I) or Tropical Rainfall Measurement Mission (TRMM) [*Krishnamurti et al.*, 1993]. They have the advantage of providing quantitative estimates of the latent heat release. The link between convective activity, brightness temperatures, and divergence fields is less direct but has the advantage of combining a larger space cover with time continuity.

In the present study, we focus on wind divergence fields over the Indian Ocean during the INDOEX period (from January to April 1999). The method for estimating vertical profiles of horizontal wind divergences from Meteosat-5 data is described in section 2. Section 3 compares these retrieved divergence fields to ECMWF fields and those derived from water vapor winds. Interests and limitations of the method are finally discussed in section 4.

2. Estimation of Divergence Profiles From Meteosat-5 Data

2.1. Principle

Narrowband measurements in the window channel (10.5-12.5 μm) have a high sensitivity to cloudiness variation and are then often used as a proxy for deep convection [e.g., *Pires et al.*, 1997]. The relations between convection and large-scale variables have been abundantly investigated. Previous studies [*Cornejo-Garrido and Stone*, 1977; *Khalsa*, 1983; *Liu*, 1988] have shown that low-level convergence must supply most of the local moisture for convection. A classical closure for convection schemes relies on this mechanism. Thus we expect to find a positive correlation between a brightness temperature in the window channel and mass convergence in the lower troposphere. Because of the continuity equation and because of the slow evolution of meteorological systems this correlation must extend after changing sign to higher levels of the troposphere.

For building correlations, instead of brightness temperatures we consider the difference $\Delta T = T_{b\mathrm{IR}} - T_{b\mathrm{IRcls}}$, between the brightness temperature $T_{b\mathrm{IR}}$ and the clear-sky brightness temperature $T_{b\mathrm{IRcls}}$, both defined in the window channel. Considering ΔT instead of $T_{b\mathrm{IR}}$ is particularly important over land, to avoid interpreting cold surface temperatures as convection. The ΔT is correlated at each model level with the normalized mass flux divergence $D = 1/\delta p \mathrm{div}(\delta p \mathbf{v})$, where δp is the pressure thickness of the layer and $\mathbf{v}$ is the horizontal wind.

2.2. Numerical Tools

Correlations between ΔT and D are computed with the atmospheric general circulation model of Laboratoire de Météorologie Dynamique (LMD), the LMDZT AGCM, a second-generation version of the LMD AGCM [*Sadourny and Laval*, 1984]. This grid point model allows the use of a variable mesh defined by coordinate stretching or "zoom," to increase resolution over any region of interest; the present zoom is a more elaborated version of the one defined by *Sharma et al.* [1987]. In this study, resolution reaches $1.3° \times 1.3°$ at the zoom center located on the equator, at 63°E, with 19 σ levels on the vertical. Convection is represented by *Tiedtke*'s [1989] scheme, and the diurnal cycle is included. The cloud scheme is described by *Le Treut and Li* [1991]. The cloud water content evolution is determined through a budget equation. A simple statistical scheme uses the assumption of a uniform distribution of the total water content within a given grid box, characterized by a width Δq_t. It allows the definition of a cloud fraction as the part of the grid surface where there is supersaturation. More details about the LMDZT AGCM are given by *Le Treut et al.* [1994], *Polcher et al.* [1991], and *Hourdin and Armengaud* [1999].

The statistics are based on 12 instantaneous simulated cases, archived for the region comprised between 30°S and 30°N, 30°E and 110°E. These cases are sampled every 12 hours from January 25, 1200 UTC, to January 31, 0000 UTC, from a simulation starting from the ECMWF analysis of January 15, 1999, 0000 UTC, and forced by observed sea surface temperatures. Dropping the first 10 days of the simulation ensures that the model is far from its spin-up phase and that convection has reached its normal regime. The choice of 12 cases in the LMDZT simulation corresponds to $\sim$ 14,000 atmospheric columns. To test the statistical significance of this ensemble, the analysis which follows was applied to two different years (January 1988 and January 1999), with practically identical results. We concentrate on the winter season, which is the INDOEX period.

Synthetic brightness temperatures are computed from the profiles of temperature, specific humidity, cloud cover, and liquid water contents sampled from the 16 day prediction run of the LMDZT AGCM. The clear-sky temperatures $T_b\mathrm{IRcls}$ are estimated by removing cloud cover and liquid water in the archived profiles. We use a modified version of the narrowband model detailed by *Morcrette and Fouquart,* [1985] and *Morcrette* [1991]. The IR and WV channels are represented with 10 spaced spectral intevals. Clouds are treated as grey bodies. This code has been extensively used at LMD for AGCM evaluation purposes [*Roca,* 1999] and was shown to give good agreement in the water vapor channel with the radiative transfer model used operationally at EUMETSAT for satellite calibration [*Roca and Picon,* 1997].

2.3. Filtering Out Semi-transparent Clouds

Filtering out semi-transparent clouds has a major impact on the correlations between ΔT and D. Indeed, high semitransparent clouds and lower opaque clouds may have the same brightness temperature in the window channel, but for very different divergence profiles. Only the opaque clouds are typical of enhanced convection and are associated with a strong convergence in the lower troposphere.

The method for this filtering has to be applicable to both simulated clouds and observed clouds. This means that some of the AGCM information, like the simulated cloud fraction profiles, cannot be used; in a similar way, radiative thresholds classicaly used with observations and defined at high spatial resolution should also be avoided because synthetic brightness temperatures cannot be computed at these fine scales.

We adopted a classical approach using a combination of the IR and the WV Meteosat channels. Indeed, the relations between radiances measured in both channels are different for opaque clouds and semitransparent clouds [*Szejwach,* 1982]. Plate 1a shows the correspondence between the observed brightness temperatures defined in the water vapor channel $T_b\mathrm{WV}$ and ΔT, for the cases defined in section 2.2, 5 km × 5 km pixels having previously been averaged and interpolated to the model grid. This diagram agrees generally well with its equivalent, produced with simulated brightness temperatures (Plate 1b), in spite of a cold bias in the WV channel of ~ 4 K, which is consistent with the AGCM validation performed by *Roca and Picon* [1997] from Meteosat-3 and Meteosat-4 WV data. This good agreement allows us to define a threshold using the radiative properties of the simulated clouds.

In the AGCM we are indeed able to distinguish between a number of simulated cloudiness classes, using cloud fractions criteria. For our purpose we retained three classes: the semitransparent clouds (STC) class and the opaque clouds (OC) class, whose characteristics are given in Figure 1, and a class of other clouds, which do not meet these criteria. The chosen criteria are somewhat arbitrary; however, they select only the extreme cases, the quasi-isolated high semitransparent clouds and the very opaque clouds which cover an important part of the model grid box. STC and OC are quite distinct on Plate 1b: The STC are roughly located along the dashed line of Plate 1b, with dense clouds at the lower left part and thin clouds at the upper right part. The OC, which behave as blackbodies, have similar brightness temperatures in both channels at high altitudes; they are located along the solid line of slope 1 for low brightness temperatures. For higher brightness temperatures or lower altitudes their WV brightness temperature saturates to the clear-sky value, whatever the exact altitude of the cloud located below the WV weighting peak function level. More details about the interpretation of this diagram are given by *Szejwach* [1982], *Schmetz et al.* [1993], and *Xu et al.* [1998].

These classes are better separated in Plate 1c, which displays the values of $(T_b\mathrm{WV}/T_b\mathrm{IR})^2$ as a function of ΔT. We then use Plate 1c to filter out the STC by defining a threshold P_{WV} as a function of ΔT (black curve in Plate 1c), from the locations of the simulated opaque clouds and the simulated semitransparent clouds. Only the points located above the curve will be considered as opaque clouds.

In order to see the effect of the selection on correlations between ΔT and D we plot in Figure 2 the values of D derived at 900 hPa versus the corresponding values of ΔT in three cases: for the whole set of points (Fig-

Class Levels (hPa)	OC	STC
6		
30		
50		at least 1 level with $neb \geq 0.3$
90		
140		
200		
280	at least 2 levels with $neb > 0.5$	
360		
450		
540		at least 5 levels with $neb < 0.05$
630		
710		
780		
850		
900	at least 4 levels with $neb > 0.5$	10 levels with $neb < 0.2$
940		
960		
980		
990		

Figure 1. Cloud fraction criteria used to define classes of simulated cloudiness. OC, opaque clouds; STC, semitransparent clouds; neb, cloud fraction value.

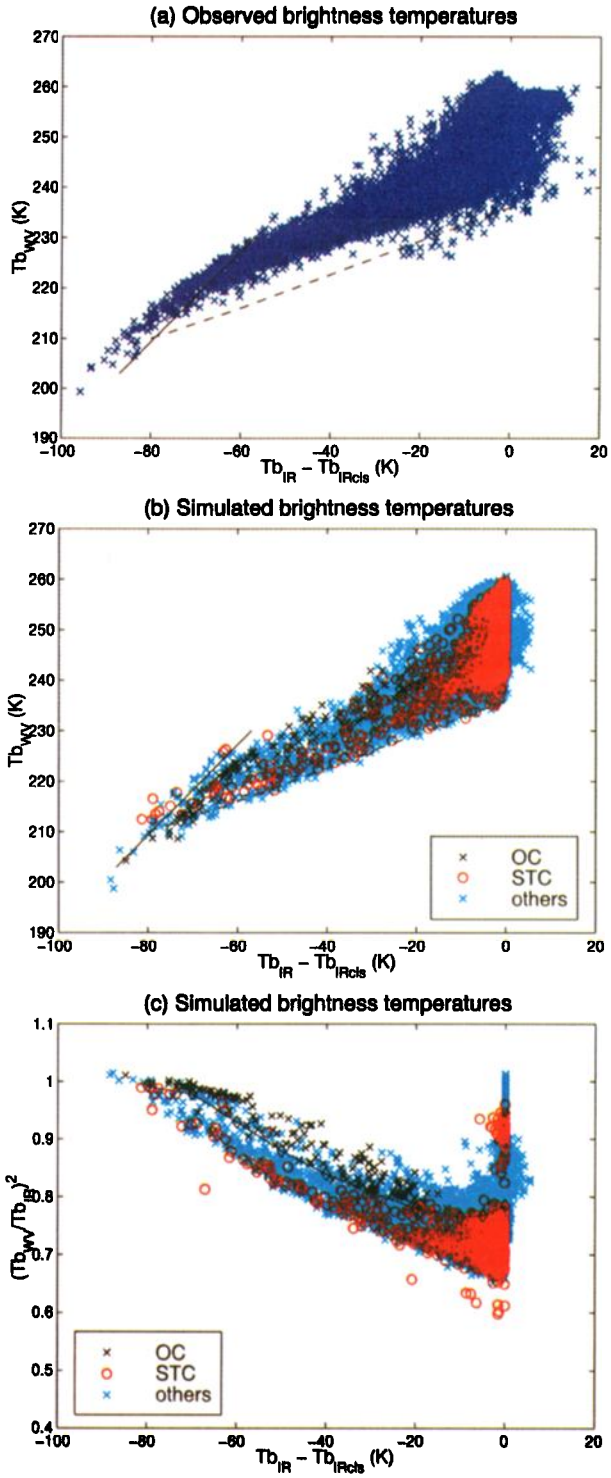

Plate 1. (a) Correspondence between the observed ΔT and $T_b\mathrm{WV}$, the brightness temperature in the water vapor channel. The 5 km × 5 km Meteosat-5 pixels have been interpolated to the model grid. (b) Correspondence between the simulated ΔT and $T_b\mathrm{WV}$. Three classes of simulated clouds are represented: opaque clouds (OC), semitransparent clouds (STC), and other clouds. (c) Scatterplot of the simulated ΔT (abscissa) versus $(T_b\mathrm{WV}/T_b\mathrm{IR})^2$ (ordinate). The STC and the OC are represented as well as the threshold curve $P_{\mathrm{wv}}(\Delta T)$.

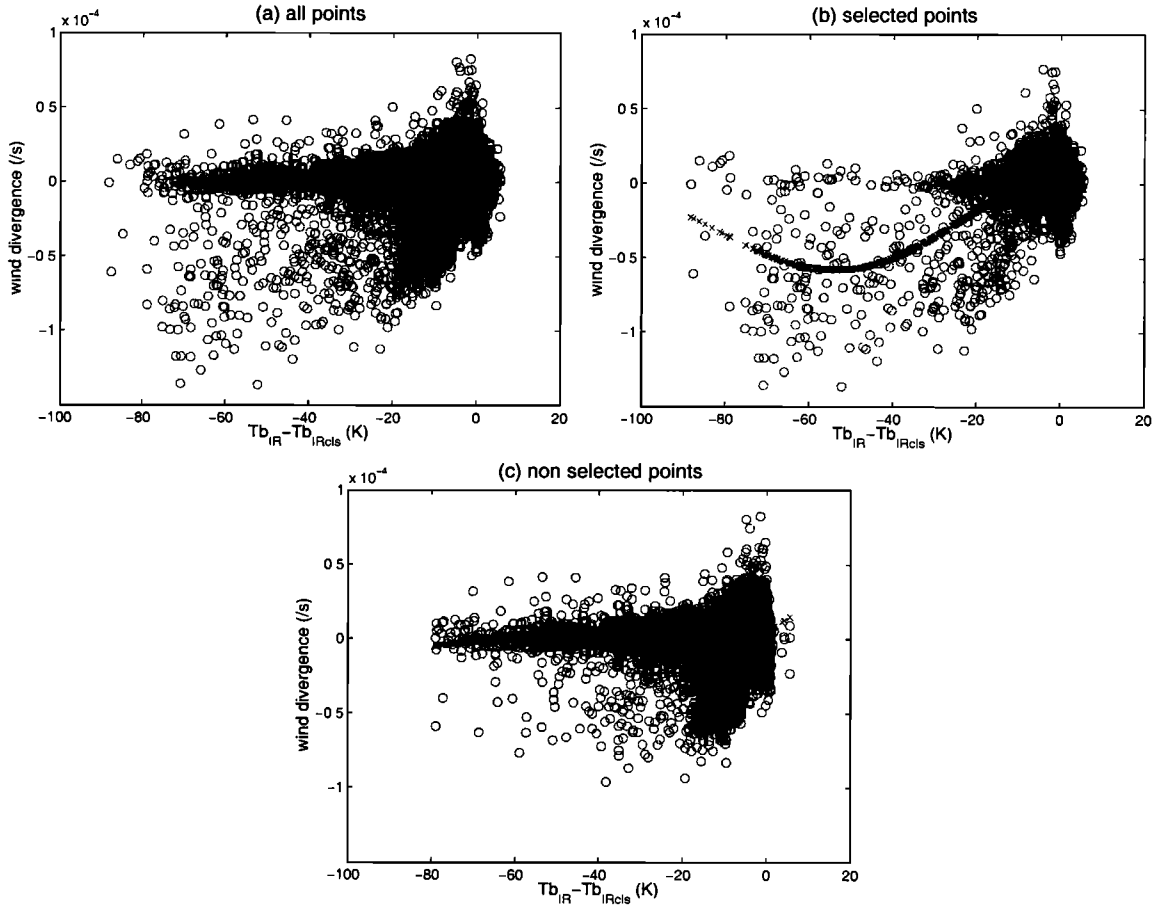

Figure 2. Scatterplots of the simulated ΔT versus D derived at 900 hPa (a) for the whole set of points, (b) for the points located above the threshold curve $P_{\mathrm{WV}}(\Delta T)$, and (c) for the points located beneath $P_{\mathrm{WV}}(\Delta T)$.

ure 2a), for the points located above $P_{\mathrm{WV}}(\Delta T)$ (Figure 2b), and for the points located under $P_{\mathrm{WV}}(\Delta T)$ (Figure 2c). Two modes clearly appear in Figure 2a. Comparison of Figures 2a,2b,and 2c shows that the threshold enables us to mostly separate the two modes (mode 1 is in Figure 2b and mode 2 in Figure 2c). It then helps in constructing a unimodal relationship between divergences and IR brightness temperature.

Figure 3 extends this conclusion to all vertical levels, displaying two vertical profiles of correlation coefficients linking variables ΔT and D, one constructed by using our selection, and the other constructed by using the whole ensemble of points. As expected, the correlation coefficients are positive in the lower troposphere, negative in the middle and upper troposphere, and weak in the stratosphere. The selection enhances their amplitude. The significance of the increase of absolute values of correlation coefficients when the selection is performed is checked performing a Student test, which is successful at a 98% level.

For application to Meteosat-5 data the threshold curve $P_{\mathrm{WV}}(\Delta T)$ is slightly modified to take into account the systematic cold bias. We checked that this threshold curve is valuable when applied to observations using a dynamical clustering method (DCM) with Meteosat-5 data (see Appendix A). At the end, divergence profiles are estimated only for points located above $P_{\mathrm{WV}}(\Delta T) = \sum_{i=0}^{4} c_i \Delta T^i$, where c_i are polynomial coefficients given in Table 1.

2.4. Retrieval of Divergence Profiles as Functions of ΔT

At each level we fit on the selected points a polynomial regression curve of degree 4, $D = f(\Delta T)$ (an example is shown in Figure 2b). Furthermore, we estimate the standard deviations of divergences for each level as functions of ΔT, to evaluate the uncertainties associated with the estimates. Figure 4 displays the divergence profiles corresponding to different brightness temperatures and the associated standard deviations. For warm brightness temperatures (300 K, or $\Delta T = 0$ K), corresponding to clear sky, a weak positive divergence is found in the lower troposphere: We indeed expect clear skies to be predominantly associated with subsidence regions. For intermediate brightness temperatures (250

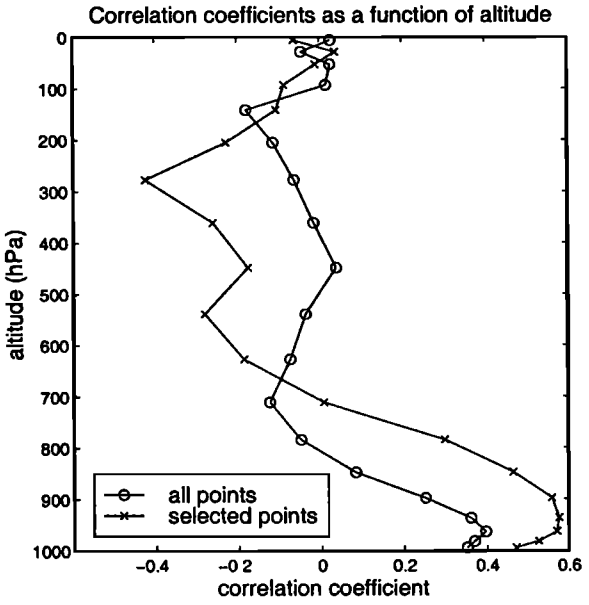

Figure 3. Vertical profiles of correlation coefficients linking variables ΔT and D, constructed using the whole set of points and using the points selected by the threshold curve only.

K, ΔT = -40 K), corresponding to shallow convection, strong convergence is noticed in the lower troposphere, while divergence occurs in the middle troposphere. For cold brightness temperatures (220 K, ΔT = -70 K), corresponding to deep convection, convergence is found in the lower troposphere up to 650 hPa, balanced by strong upper tropospheric divergence. Note that the -40 K and -70 K cases differ by the level of detrainment, rather than by the intensity of the lower convergence.

To test the dependence of the retrieved divergence profiles on the convection scheme, the same operations were performed, using the original convection scheme of the LMD AGCM [*Sadourny and Laval,* 1984]. The LMD AGCM applies successively a moisture adjustment procedure for eliminating conditional instability when saturation occurs [*Manabe et al.,* 1965] and the *Kuo* [1965] scheme, which takes into account large-scale water vapor convergence and evaporation from the surface, to force convection and to enable the vertical mixing of energy and water. This successive application we refer to as the Kuo-Manabe scheme.

The retrieved divergence profiles exhibit the same qualitative characteristics with the two convection scheme (Figure 5). However, the absolute values of D obtained with the Kuo-Manabe scheme are weaker. When ΔT is equal to -40 K, the mean value of D beneath 940 hPa obtained with the Kuo-Manabe scheme is on the order of $-3.5 \times 10^{-5}s^{-1}$, instead of $-5 \times 10^{-5}s^{-1}$ with *Tiedtke*'s [1989] scheme. Thus the use of different parameterizations of convection implies quantitative differences for the retrieval of divergences. In the rest of the paper, only Tiedtke's scheme is used.

2.5. Validation of the Method

To validate our method, we first performed a retrieval from simulated brightness temperatures and compared the retrieved divergences with the initial divergences (ID) of the AGCM run. Over the convective areas, characterized by weak brightness temperatures in Figure 6, the values of convergence in the lower troposphere (940 hPa) are usually well retrieved. The cold structure found near 90°E; 20°S is not selected for the divergence retrieval; Indeed, the cloud fraction profiles of this area exhibit a low cloud at 850 hPa, covering $\sim$ 40% of the mesh, associated with a cirrus at 200 hPa, whose cloud fraction is high. This type of cloud system must be eliminated for the retrieval, as it should not be interpreted as a unique intermediate opaque cloud.

We quantitatively estimated the agreements of the retrieved divergences with the initial divergences, taking into account the uncertainty in the divergence estimate due to the statistical dispersion in Figure 4. An agreement between two divergences is considered as good if the initial divergence falls within the error bar associated with the estimated divergence. (Note that the error bars, defined at the standard deviations of simulated divergences, are also clearly model dependent.) The derivation of agreements are performed over the 12 instantaneous simulated cases; percentiles of agreements are then deduced from this data set (see Figure 7).

The mean agreement is equal to 40%. This value has to be compared to 38%, the probability for a random variable of Gaussian distribution to be equal to its mean value at 1σ level. No particular pattern appears on the graph; for altitudes and ΔT values associated with a large amplitude of the retrieved divergences, the agreements are close to their mean value (28% - 50% beneath 940 hPa, for ΔT lower than -50 K).

3. Application to Meteosat-5 Data: Comparison With ECMWF Divergences and Divergences Derived From EUMETSAT Winds

In this section, Meteosat-5 images recorded in January 1999 during the INDOEX experiment are analyzed. The estimated divergences are compared with

Table 1. Definition of the Threshold Curve P_{WV}

	Value
c_5	$4.1798\ 10^{-10}$
c_4	$8.0922\ 10^{-8}$
c_3	$6.0437\ 10^{-6}$
c_2	$2.4111\ 10^{-4}$
c_1	$1.7664\ 10^{-3}$
c_0	0.7846

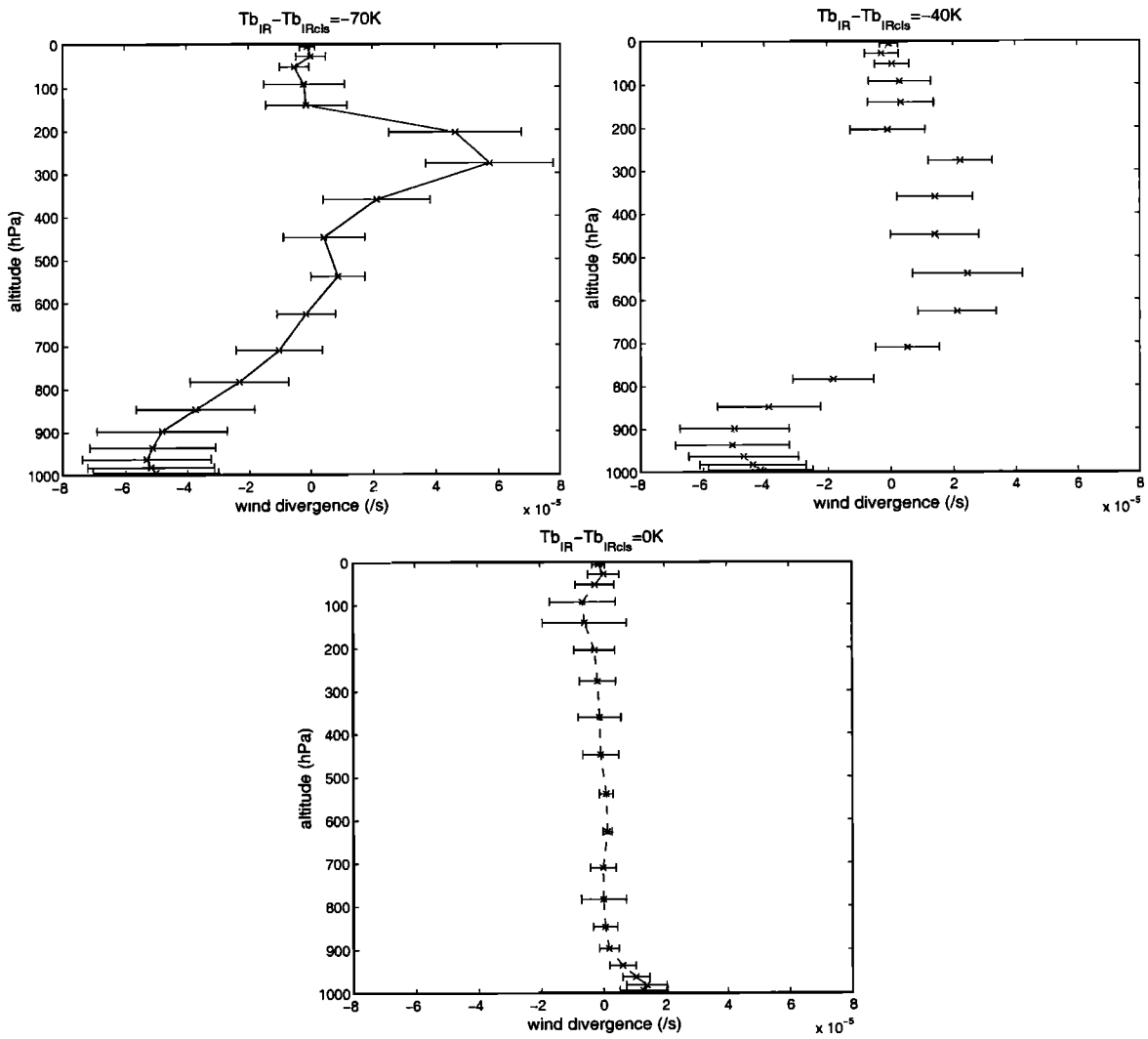

Figure 4. Vertical profiles of D computed with *Tiedtke*'s [1989] scheme, for selected points, corresponding to ΔT values of -70 K (solid curve), -40 K (dotted curve) , and 0 K (dashed curve).

ECMWF divergences and divergences derived from WV winds, corresponding to the same period.

3.1. ECMWF Divergences

We use directly the ECMWF divergence fields. These divergences are computed from ECMWF analyses of winds, performed every 6 hours by the ECMWF global numerical weather prediction (NWP) model. This model has a 62 km Gaussian grid, with 60 vertical levels defined in a hybrid sigma-pressure coordinate. A four-dimensional (4-D) variational assimilation method is used to ingest radiosonde and satellite winds. The satellite winds are IR, WV, and VIS Meteosat-5 and Meteosat-7 winds, defined with a 90 min time sampling and at a resolution of 160 km, high-resolution VIS Meteosat-5 and Meteosat-7 winds, defined with a 3 hour time sampling and at a resolution of 80 km, and GOES winds, defined with a 3 hour time sampling. Here the divergences are computed on the first 31 model levels, at a horizontal resolution of $0.5^o \times 0.5^o$. To make the ECMWF divergences (ECD) comparable with the divergences retrieved from brightness temperatures (BTD), we perform vertical and horizontal interpolations of the divergences on the variable mesh of the AGCM.

3.2. Estimation of Divergences Derived From EUMETSAT Winds

We use here the EUMETSAT operational WV winds, available at a spatial resolution of 160 km. They are computed from semihourly images in the Meteosat WV channel at full resolution (5 km × 5 km at the subsatellite point). The WV wind extraction procedure, described by *Laurent* [1993], is based on a window technique. A small window, named target window at time t, searches inside another window placed at time $t - 30$ min or $t+30$ min for a similar pattern. The temperature of the tracer is estimated by analyzing its distribution

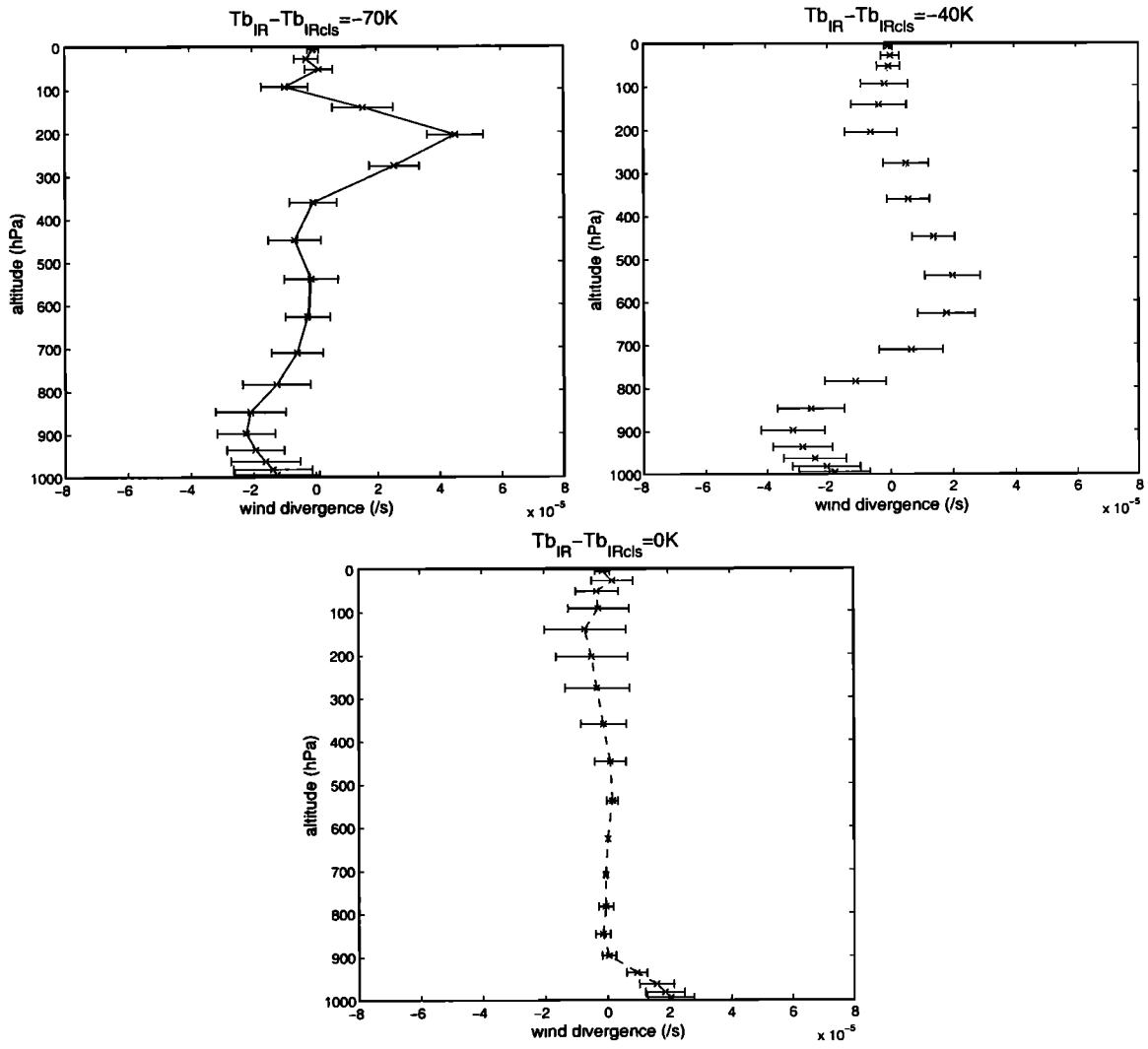

Figure 5. As in Figure 4, except that the vertical profiles are computed with the Kuo-Manabe scheme.

of WV and IR pixels, following *Schmetz et al.* [1993]. Then the altitude is assigned using temperature and pressure profiles of the ECMWF forecast.

Computation of divergence from water vapor winds is a delicate matter, divergence being selective of small scales. Here, following *Laurent and Sakamoto* [1998], winds are first interpolated on a regular grid ($1.2^o \times 1.2^o$) in both space and time, with a technique proposed by *Doswell* [1977]. The value Φ_0 assigned to a location M_0 at time t_0 is defined as the weighted average of the values Φ_i, observed at locations M_i and times t_i:

$$\Phi_0 = \frac{\sum_{i=1}^{M} W_i \Phi_i}{\sum_{i=1}^{M} W_i}, \tag{1}$$

where W_i are weights depending on distances $d_i = M_0 M_i$ and time lags $\Delta t_i = t_i - t_0$

$$W_i = \exp\left(-(d_i/\delta)^2 - (\Delta t_i/\tau)^2\right). \tag{2}$$

The parameters δ and τ must be adjusted in order to filter small-scale frequencies in space and time, respectively, without affecting large-scale structures. After some tests, τ and δ were fixed at 90 min and 279 km, respectively.

Horizontally, the WV wind field defined on the $1.2^o \times 1.2^o$ grid is interpolated on the AGCM grid, which is an Arakawa type C grid [*Kasahara*, 1977], where zonal wind, meridional wind, and scalar variables are defined at three different locations on the mesh. Vertically, each wind is affected to the closest model level (defined in sigma coordinate $\sigma = p/p_s$), using its pressure level given in the EUMETSAT data and the surface pressure of ECMWF. The WV divergences (WVD) are derived from winds defined on the model grid and ECMWF surface pressure, following the expression of D given in section 2.1.

3.3. Case Study

The results presented here are related to two Meteosat-5 images recorded on January 15, 1999, at 1200 UTC and on January 25, 1999, at 1200 UTC, characteristic

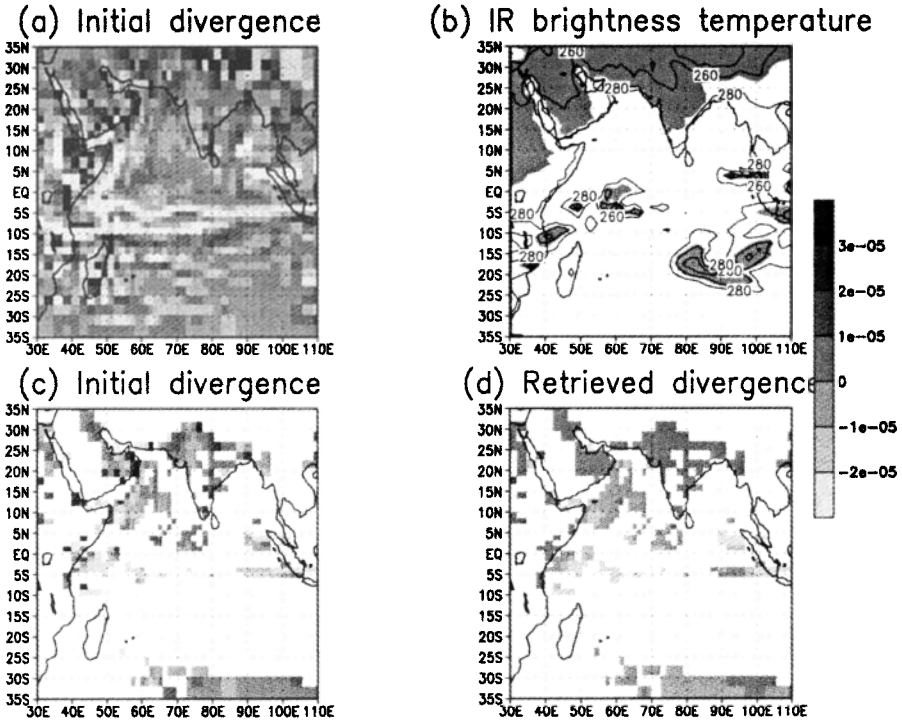

Figure 6. (a) Initial divergence field at 940 hPa computed with the AGCM, (b) Simulated IR brightness temperatures for the same field, (c) Same as Figure 6a, but with the mask of Figure 6d, (d) Retrieved divergence field at 940 hPa.

of the variability of convective areas. Figure 8 shows the spatial distributions of IR brightness temperatures, where pixels have been averaged and interpolated on the model grid. On January 15, three main convective cloud systems are found, located near 70°E to 5°S, 105°E to 5°S, and 35°E to 10°S; another cold pattern of approximately 250 K appears over Arabia. On January 25 the convective patterns globally shifted from the middle to the eastern part of the ocean, an effect attributable to the Madden-Julian oscillation. The western pattern persists over East Africa and Madagascar, while a large convective system is found near the equator, between 75°E and 110°E.

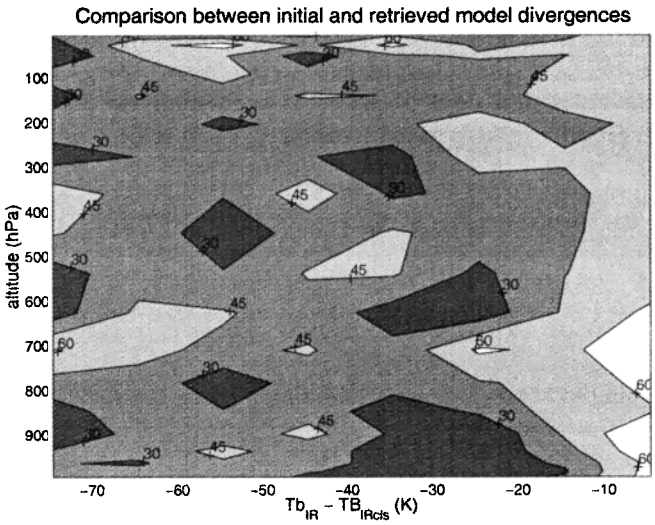

Figure 7. Percentile of agreement of brightness temperature divergences (BTD) with initial divergences, as a function of ΔT (abscissa) and altitude (ordinate).

The corresponding WVD, BTD, and ECD are represented at three different levels (360 hPa, 280 hPa, and 200 hPa) in Figures 9, 10, and 11. The unshaded areas of Figures 9 and 10 are free of data, either because they correspond to points which have not been selected for the BTD retrieval or because no water vapor wind was found at that level. Indeed, water vapor winds are estimated at one level at most, this level depending on the location and being the highest among those where water vapor is detected.

In general, for the three fields the main convective structures are associated with positive divergences. For WVD they appear at the highest level (200 hPa), whereas the objects tracked around these cloud systems are usually found at the intermediate level (280 hPa), and most of the warm areas are observed at a lower level (360 hPa). The shapes and the locations of the positive structures of divergences are similar on WVD and on BTD fields; however, the ECD exhibit some differences, especially on January 25. The BTD values over the convective areas are on the same order of magnitude as the ECD values (they reach $5 \times 10^{-5}s^{-1}$ at 200 hPa) but are larger than those of the WVD (which are between 1×10^{-5} and $4 \times 10^{-5}s^{-1}$ at 200 hPa). However, the WVD values are quite dependent on the spatial smoothing. If performed at a smaller scale, the

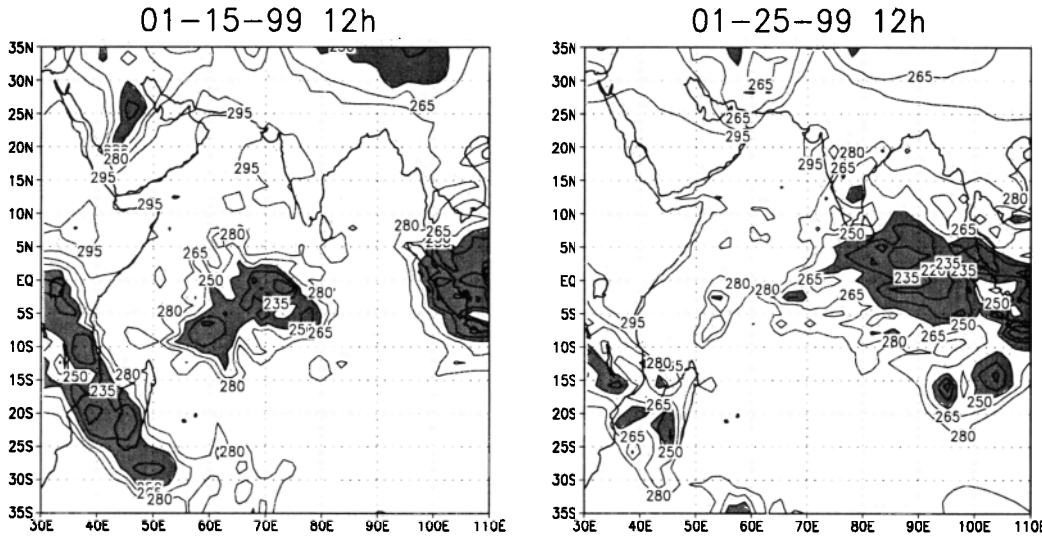

Figure 8. The spatial distribution of IR Meteosat-5 brightness temperatures in the window channel: on January 15, 1999, at 1200 UTC and on January 25, 1999, at 1200 UTC (values lower than 250 K are shaded).

smoothing is not efficient in eliminating the noise, but most of the positive WVD increase and the agreement between WVD and BTD becomes better.

The relation noticed in section 2.4 between the level of detrainment and the brightness temperature is here validated by the WVD fields. Indeed, the intermediate brightness temperature of 250 K found over Arabia on January 15 is associated with a positive divergence which occurs at a lower level than divergence related to deep convective clouds, as well on WVD as on BTD fields. The ECD fields exhibit a weaker vertical correlation than the BTD.

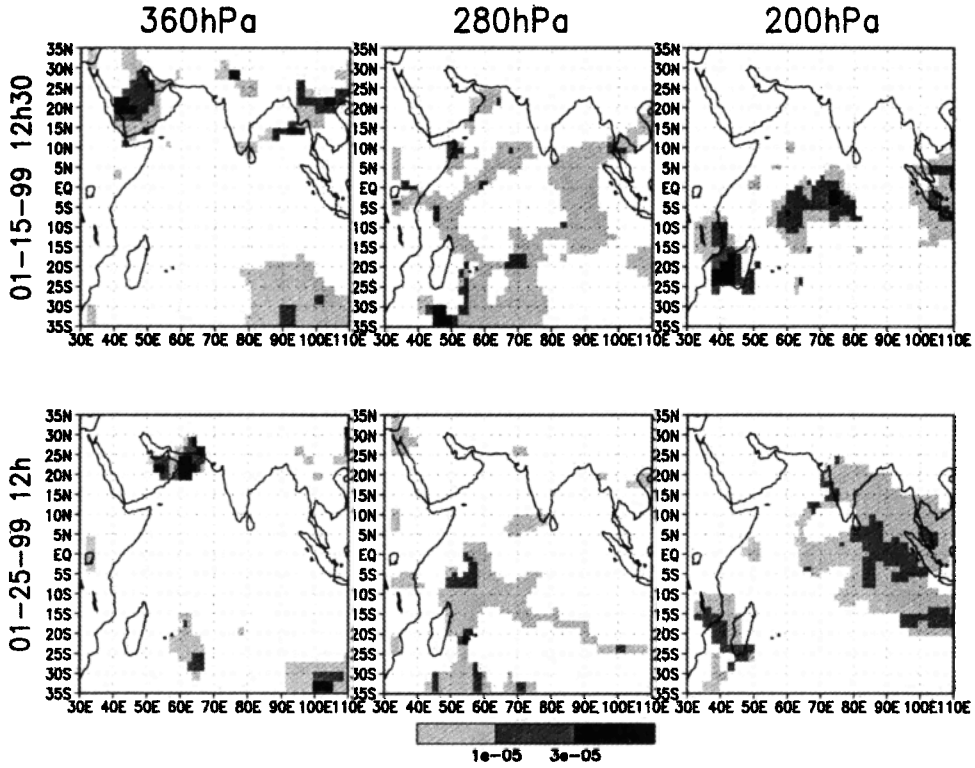

Figure 9. Divergences derived from water vapor winds, with the spatial smoothing parameter δ = 270 km and interpolated to the model grid. Upper row, January 15, 1999, at 1230 UTC; lower row, January 25, 1999, at 1200 UTC; left column, 360 hPa ; middle column, 280 hPa; right column, 200 hPa.

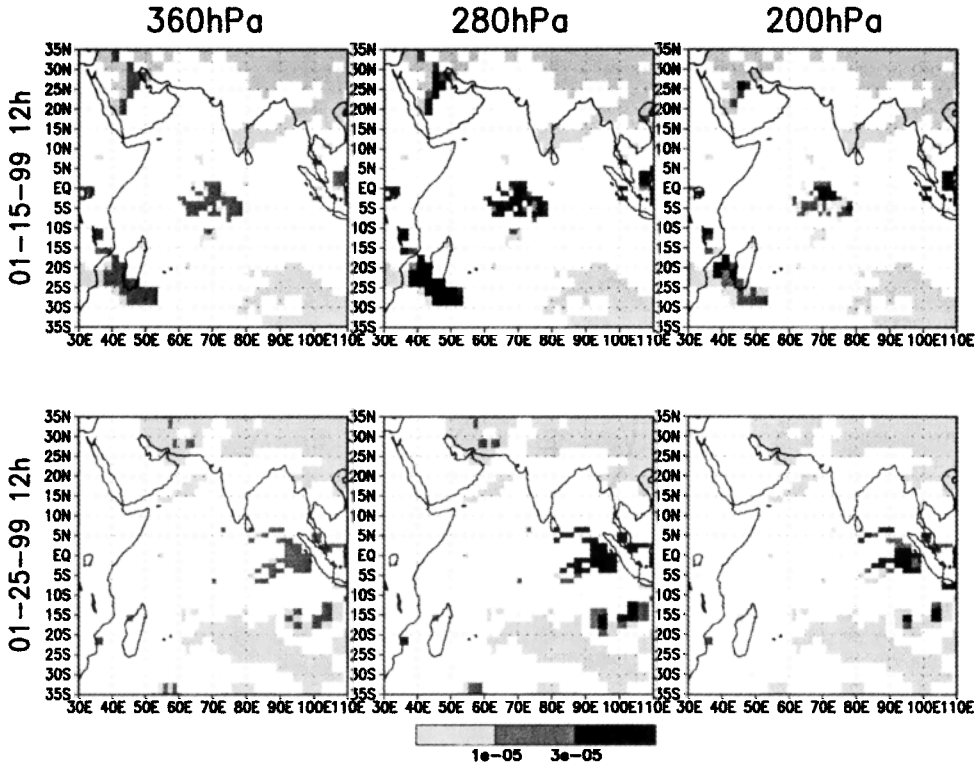

Figure 10. Divergences estimated from IR Meteosat-5 brightness temperatures. Upper row, January 15, 1999, at 1200 UTC; lower row, January 25, 1999, at 1200 UTC; left column, 360 hPa; middle column, 280 hPa; right column, 200 hPa.

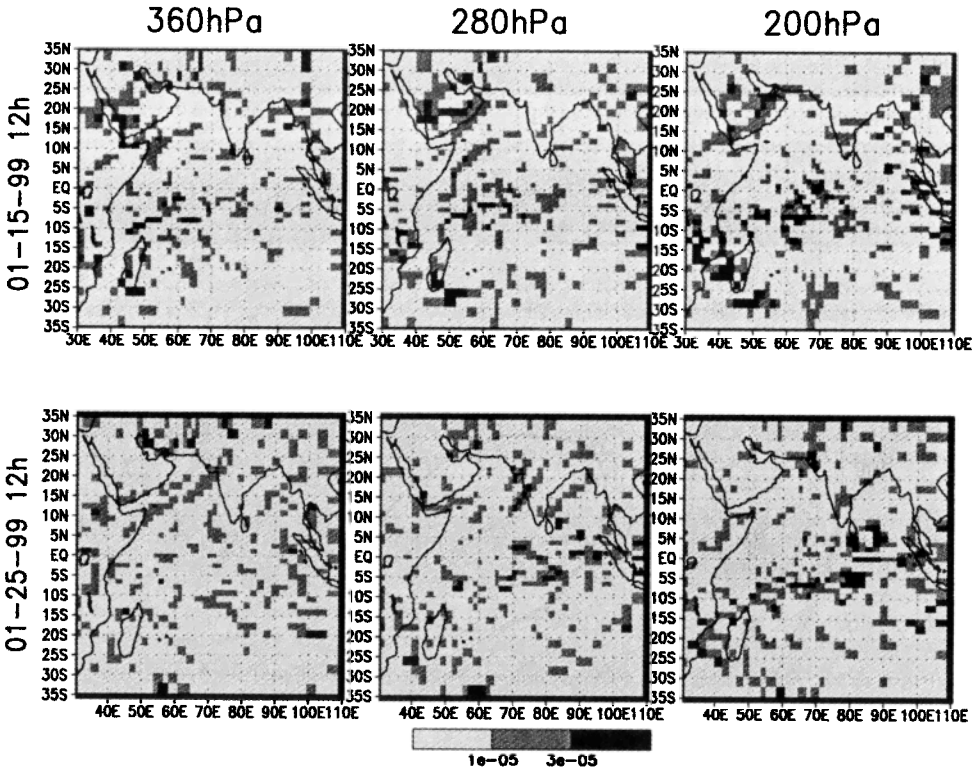

Figure 11. ECMWF divergences. Upper row, January 15, 1999, at 1200 UTC; lower row, January 25, 1999, at 1200 UTC; left column, 360 hPa; middle column, 280 hPa; right column, 200 hPa.

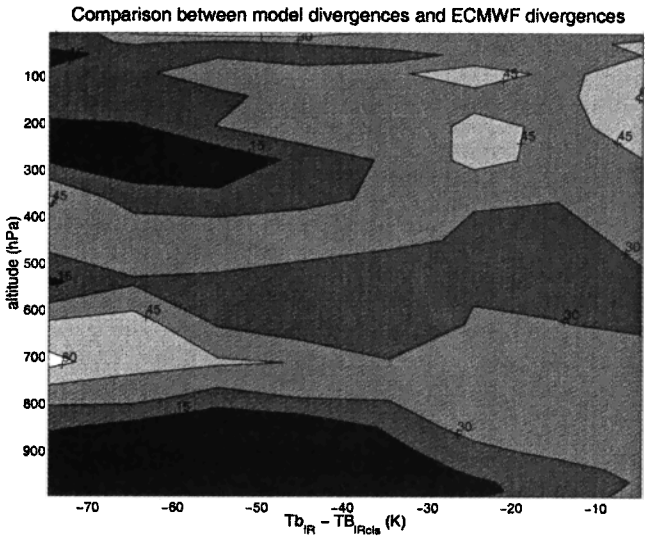

Figure 12. Percentile of agreement of BTD with ECMWF divergences, as a function of ΔT (abscissa) and altitude (ordinate).

3.4. Statistics

Here we estimate the agreements of WVD and ECD with BTD, taking into account the uncertainty in the divergence estimate due to the statistical dispersion in Figure 4. As in section 2.5, an agreement between two divergences is considered good if the WVD or the ECD falls within the error bar associated with the estimated BTD. The derivation of agreements is performed over 12 instantaneous cases of January 1999, and percentiles of agreements are derived from this data set.

The percentiles of agreement of BTD with ECD are represented in Figure 12 as a function of ΔT and altitude. The agreement is $\sim$ 40% for warm temperatures. It is much weaker over convective areas, at the altitudes where the BTD profiles exhibit a large amplitude. Indeed, in the lower troposphere for intermediate and cold temperatures, in the middle troposphere for intermediate temperatures, and in the upper troposphere for cold temperatures it is sometimes lower than 15%, which is much weaker than the values found in these cases for the reconstruction of divergences from simulated brightness temperatures (section 2.5). Thus the ECD are significantly different from the divergences predicted by the LMDZT AGCM in convective situations.

Statistical comparisons with WVD can be performed for the upper level only. In Figure 13a we first compare the BTD with the WVD defined at the same levels, at 200 hPa, 280 hPa, or 360 hPa (solid curve). A weak agreement (9%) is found for ΔT lower than -70 K; how-

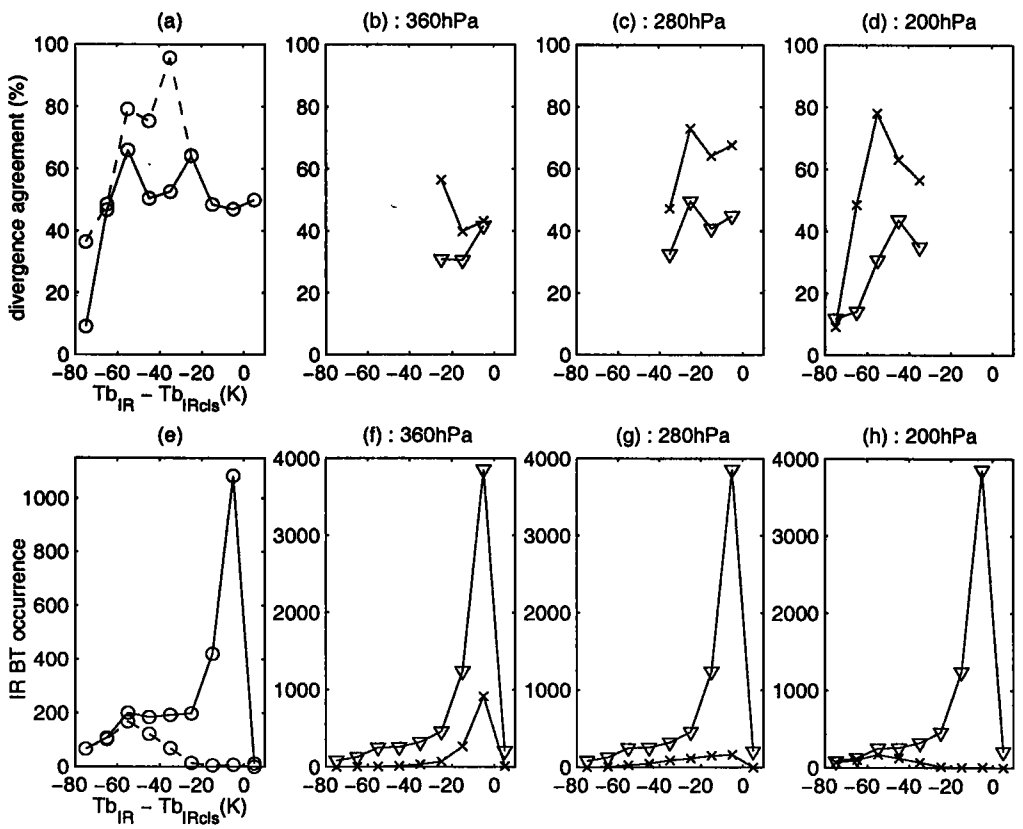

Figure 13. Upper row (a) BTD-WVD agreements, as a function of ΔT. The solid curve is constructed by comparing BTD with WVD defined at the same levels (200 hPa, 280 hPa, and 360 hPa). The dashed curve is constructed by comparing WVD found at 200 hPa with BTD of 200 hPa or 280 hPa (b), Comparison at 360 hPa of BTD-WVD agreements (curve with crosses) with BTD-ECD agreements (curve with triangles). (c) : same as Figure 13b, but at 280 hPa. (d), same as Figure 13b, but at 200 hPa. (e-h) IR brightness temperature occurence, for reference; in each case, number of divergence pairs as a function of ΔT

ever, values extend from 47% to 66% for ΔT warmer than -70 K. The dashed curve is built by comparing WVD found at 200 hPa with BTD at either 200 hPa or 280 hPa. In this case, a good agreement is found if the WVD at 200 hPa falls within at least one of the error bars of BTD associated with the 200 hPa and the 280 hPa levels. This relaxation of the vertical constraint significantly increases the agreement. It reaches 36% for ΔT lower than -70 K and extends from 75% to 96% in the -60 K to -30 K interval. For ΔT warmer than -20 K, agreements are not represented, the total number of divergence pairs found in the high troposphere at these temperatures being very low (Figure 13e).

Thus there is generally good agreement between the BTD and the WVD fields over convective areas. Indeed, the major convective patterns usually have similar shapes and locations. This comparison of high-level divergences constitutes, then, a partial validation of our divergence estimation over convective areas, and the EUMETSAT products confirm the link expected between horizontal wind divergence and convective structures. The low agreement found for ΔT lower than -70 K can be attributable to the spatial smoothing of the WV winds which underestimate the divergence values. In a further step, it would be interesting to use the high-resolution WV winds (having a spatial resolution of 80 km instead of 160 km). This product is operationally available and would provide a better horizontal cover and a more accurate estimation of WV divergences.

Finally, Figures 13b, 13c and 13d show a comparison of BTD-WVD agreements with BTD-ECD agreements at the three levels, in the cases where the number of WVD-BTD pairs is large enough to get significant results. The BTD agree better with the WVD than with the ECD for all altitudes and temperatures, and this good agreement is more pronounced for cold ΔT. The differences between ECD and WVD over convective cases, while ECMWF assimilates the same WV cloud motion winds as those used to compute WVD, can arise either from errors due to the space and time interpolation performed on WV wind fields or from the impact of assimilating other variables in the ECMWF analyses. The differences between ECD and BTD can be due to the fact that ECMWF does not use brightness temperatures, but only WV winds, in their assimilation process; futhermore, ECMWF mixes Meteosat-5 data with all data available, while our approach concentrates on reconstructing divergences from brightness temperatures.

4. Discussion and Conclusion

This study describes the retrieval of horizontal wind divergences from infrared satellite imagery data. The method is partially validated by comparison with water vapor divergence fields. The vertical profiles of divergence associated with convection constitute an interesting diagnostic tool which it would be worthwhile to apply to additional observations and to different convection schemes. This would assess these schemes and document the relation between air convergence in the lower troposphere and enhancement of convection.

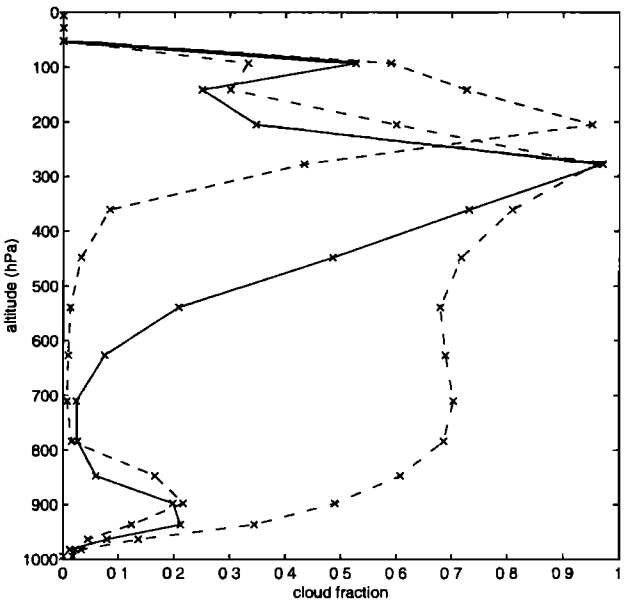

Figure 14. Mean vertical profiles of cloud fractions for $-70\text{K} \leq \Delta T \leq -50\text{K}$. The profiles correspond to the following: the points located above P_{WV} and belonging to mode 2 (solid curve), the points located above P_{WV} and belonging to mode 1 (dashed-dotted curve), and the points located below P_{WV} and belonging to mode 2 (dashed curve)

The main limitation of our divergence retrieval is the need for filtering out semitransparent clouds to reduce the uncertainty of the estimates. Mode 1 and mode 2 (section 2.3) are not totally separated by the filtering, because the radiative threshold method fails in eliminating completely clouds which do not belong to the OC class. Indeed, the clouds or systems of clouds which are not eliminated but still belong to mode 2 (we label them "pseudo-OC") are usually thick cirrus or multi layer clouds. The typical vertical profile of cloud fractions of these points is represented in Figure 14. As a comparison, the cloud fraction profile of the selected points which belong to mode 1, as well as the cloud fractions profile of the eliminated points which belong to mode 2, are also plotted in Figure 14. This shows that the "pseudo-OC" are definetely different from the convective towers and are also thicker than the semitransparent clouds. The water vapor radiative threshold method is not efficient enough to discriminate them.

The study using the dynamical clustering method (Appendix A) confirms this conclusion and extends it to the observations: It appears that $\sim$ 40% of the pixels labeled as thick cirrus and multi layer systems, detected using the infrared and the visible channels, are not eliminated with the water vapor radiative threshold method.

Thus a possible improvement of our method would be the use of the visible channel of Meteosat-5. A threshold

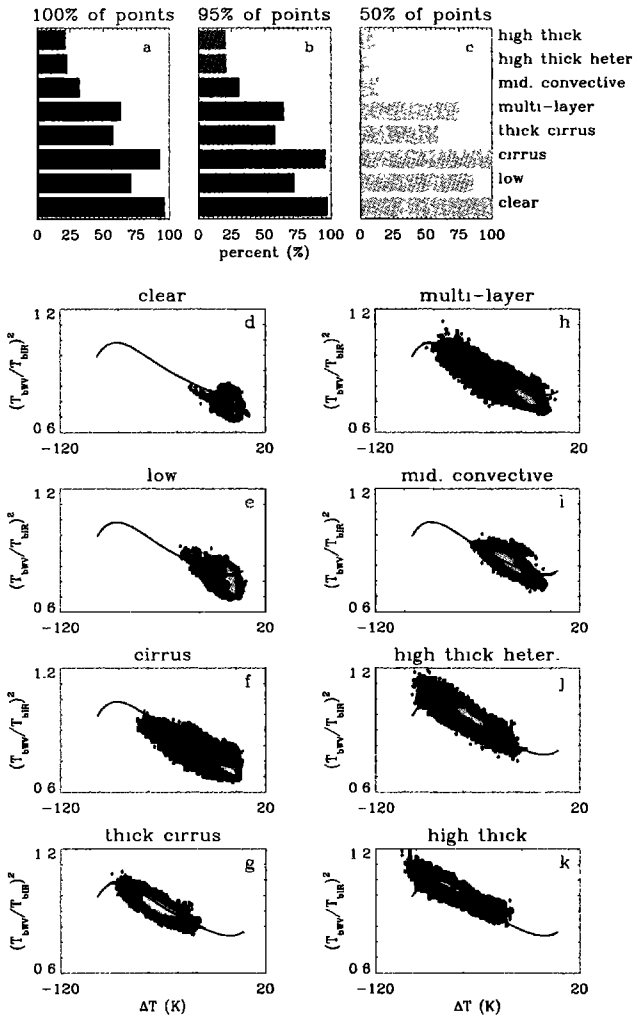

Figure 15. Results of the dynamical clustering method applied to Meteosat-5 data. (a-c) Percentiles of pixels located beneath the threshold curve $P_{WV}(\Delta T)$, for the eight classes of clouds and for 100%, 95%, and 50% of the pixels belonging to the highest-density part of the distribution. (d-k) Scatterplots of ΔT versus $(T_bWV/T_bIR)^2$ corresponding to each class. $P_{WV}(\Delta T)$ is represented, as well as the isodensities of 95% and 50%.

based on reflectance should be defined, the reflectance being dependent on the optical thickness of the cloud [*Minnis and Harrison,* 1984; *Minnis et al.,* 1984]. One disadvantage of the method is that it can be used only during daytime; furthermore, it should need accurate treatment of angular dependence. Visible information can also be used at a higher resolution (which could reach the pixel resolution). The detection of thick cirrus and multi layer systems would certainly improve much, using thresholds similar to those used in the dynamical clustering method (Appendix A). However, the problem with that approach is that we would have to simulate synthetic brightness temperatures at scales much smaller than the model mesh scale or to select the simulated clouds using a criterion different from the one used for the observed clouds.

The important differences found between ECD and BTD suggest that the Meteosat IR brightness temperatures contain useful information on divergence, which is for the moment non exploited in the ECMWF analyses but which could be used to better locate the convective systems. This information could be ingested by two different methods: by a direct 4-D VAR assimilation of brightness temperatures or by an assimilation of divergence fields deduced from correlations with brightness temperatures. The first method is more straightforward and potentially more powerful. However, it requires inversion (through adjoint integration) of a very complex direct model, including large-scale transport of water vapor, convection, and cloud schemes. The second method, which we plan to investigate, avoids some of these difficulties, because it implicitely reduces enhancement of convection to the presence of air mass convergence in the lower troposphere, relying on the AGCM behavior in its climatic mode.

In both methods the characteristics of the models, especially those of the convection schemes, are taken into account to better represent convection. This helps to reduce the "spin-up," which affects LMDZT AGCM simulations initialized by the ECMWF analyses, because of additional interpolations and substitution of one model for another. The last method is now being applied to a simulation of the INDOEX Intensive Field Phase, including tracer transport and vertical mixing by convection over the Indian Ocean Intertropical Convergence Zone (ITCZ). We expect that a more realistic ITCZ will improve the simulation of horizontal transport and vertical mixing.

Appendix A: Validation of the Selection

A weakness of our selection lies in the fact that the threshold curve is defined on the radiative characteristics of simulated clouds, the simulated clouds themselves being defined on arbitrary criteria. In order to secure that the threshold curve is valuable when applied to observations, the dynamical clustering method [*Sèze and Desbois,* 1987] has been applied to full resolution Meteosat-5 data. The aim of this method is to identify cloudiness, making use of two spectral parameters, the infrared and the visible radiances, and two structural parameters, the local spatial standard deviations of the visible and infrared radiances (computed for 3 × 3 neighboring pixels). This method is particularly interesting for our purpose as it uses the additional information of the visible channel. The infrared radiances give information on cloud altitude, whereas the visible radiances give information on the cloud optical thickness. The spatial local standard deviations associated with the IR and the visible radiances allow us to distinguish between high thick clouds, cirrus, and cirrus above other clouds and between thin cirrus and small cumulus.

The method references 20 classes of cloudiness, which are then grouped into 8 classes (Figure 15). For five Meteosat-5 pictures, taken at 12 00 LT from January 25, 1999, to January 29, 1999, each pixel over the ocean has been identified as belonging to one of the eight classes. The IR clear-sky brightness temperatures corresponding to these dates have been computed using the ECMWF temperature and specific humidity profiles. We attribute to each pixel the IR clear-sky value of the model mesh which contains it. Then for each class, a graph is built giving $(T_b\mathrm{WV}/T_b\mathrm{IR})^2$ as a function of ΔT. The percentile of pixels located above the threshold curve is derived, for the whole distribution and then for 95% and 50% of the pixels belonging to the highest-density part of the distribution.

The results show that 92% of the pixels identified as cirrus are located beneath the threshold curve, while 69% of the middle convective clouds, 78% of the high thick heterogeneous clouds, and 79% of the high thick clouds are located above the curve. Thus the threshold method is globally validated. However, only 57% of the thick cirrus and 63% of the multi layer clouds are located beneath the curve. Thus the risk of interpreting multi layer systems and thick cirrus as opaque clouds exists when the visible channel is not used; as discussed in section 4, it certainly constitutes an important part of the error associated with the retrieval.

Acknowledgments. We thank J.-J. Morcrette for making the radiative transfer code available to us and R. Roca for useful contribution concerning the radiance simulation at an early stage of this study. We are also grateful to Frédérique Chéruy and Sandrine Bony for useful discussion.

References

Cornejo-Garrido, A., and P. Stone, On the heat balance of the walker circulation, *J. Atmos. Sci.*, *34*, 1155–1162, 1977.

Doswell, C., Obtaining meteorologically significant surface divergence fields through the filtering property of objective analysis, *Mon. Weather. Rev.*, *105*, 885–892,1977.

Hourdin, F., and A. Armengaud, The use of finite-volume methods for atmospheric advection of trace species, part 1, Test of various formulations in a general circulation model, *Mon. Weather. Rev.*, *127*, 822–837, 1999.

Kasahara, A., Computational aspects of numerical models for weather prediction and climate simulation, *Meth. Comput. Phys.*, *17*, 1-66, 1977.

Khalsa, S., The role of sea surface temperature in large-scale air-sea interaction, *Mon. Weather. Rev.*, *111*, 954–966, 1983.

Krishnamurti, T., J. Xue, H. Bedi, K. Ingles, and D. Oosterhof, Physical initialization for numerical weather prediction over the tropics, *Tellus*, *43 Ser. B*, 53–81, 1991.

Krishnamurti, T., H. Bedi, and K. Ingles, Physical initialization using ssm/i rain rates, *Tellus*, *45 Ser. A*, 247–269, 1993.

Kuo, H., On formation and intensification of tropical cyclones through latent heat release by cumulus convection, *J. Atmos. Sci.*, *22*, 40–63, 1965.

Laurent, H., Wind extraction from meteosat water vapor channel image data, *J. Appl. Meteorolo.*, *32*, 1124–1133, 1993.

Laurent, H., and S. Sakamoto, Measure of divergence at the top of tropical convective systems from water vapor winds, in *Fourth International Winds Worshop, EUMETSAT Publ. EUM. P 24*, pp. 155-161, Darmstadt, Germany, 1998.

Le Treut, H., and Z.-X. Li, Sensitivity of an atmospheric general circulation model to prescribed sst changes: Feedback effects associated with the simulation of cloud optical properties, *Clim. Dyn.*, *5*, 175–187, 1991.

Le Treut, H., Z. Li, and M. Forichon, Sensitivity of the lmd general circulation model to greenhouse forcing associated with two different cloud water parametrizations, *J. Clim.*, *7*, 1827–1841, 1994.

Liu, W., Moisture and latent heat flux variabilities in the tropical pacific derived from satellite data, *J. Geophys. Res.*, *93*, 6749–6760, 1988.

Manabe, S., J. Smagorinsky, and R. Strickler, Simulated climatology of a general circulation model with a hydrologic cycle, *Mon. Weather Rev.*, *93*, 769–798, 1965.

Minnis, P., and E. Harrison, Diurnal variability of regional cloud and clear-sky radiative parameters derived from goes data, part i, Analysis method, *J. Clim. Appl. Meteorolo.*, *23*, 993-1011, 1984.

Minnis, P., E. Harrison, and G. Gibson, Cloud cover over the equatorial eastern pacific derived from july 1983 international satellite cloud climatology project data using a hybrid bispectral threshold, *J. Geophys. Res.*, *92*, 4051-4078, 1987.

Morcrette, J., Evaluation of model-generated cloudiness: Satellite observed and model-generated diurnal variability of brightness temperature, *Mon. Weather Rev.*, *119*, 1205-1224, 1991.

Morcrette, J., and Y. Fouquart, On systematic errors in parametrized calculations of longwave radiation transfer, *Q. J. R. Meteorol. Soc.*, *111*, 691–708, 1985.

Pires, P., J.-L. Redelsperger, and J.-P. Lafore, Equatorial atmospheric waves and their association to convection, *Mon. Weather Rev.*, *125*, 1167–1173, 1997.

Polcher, J., et al., Le cycle 5 du modèle de circulation générale du lmd, *Tech. Rep. LMD Internal Note 170*, Lab. de Météorol. Dyn., École Normale Supér., Paris, 1991.

Roca, R., Contribution à l'étude de la vapeur d'eau, de la convection et de leurs intéractions dans les tropiques, Ph.D. thesis, Univ. Paris VII, 1999.

Roca, R., and L. Picon, Climatic studies and gcm validation using meteosat water vapor channel data, in *Proceedings of the 1997 Meteorological Satellite Data User's Conference, EUMETSAT Publ. EUM P 24*, pp. 61-66, Darmstadt, Germany, 1997.

Sadourny, R., and K. Laval, January and July performance of the LMD general circulation model, in *New Perspectives in Climate Modelling*, edited by A. Berger and C. Nicolis, pp. 173–198, Elsevier Sci., New York, 1984.

Schmetz, J., K. H. J. Holmlund, B. Strauss, B. Mason, V. Gaertner, A. Koch, and L. Van De Berg, Operational cloud-motion winds from meteosat infrared images, *J. Appl. Meteorol.*, *32*, 1206–1223, 1993.

Sèze, G., and M. Desbois, Cloud cover analysis from satellite imagery using spatial and temporal characteristics of the data, *J. Clim.*, *26*, 287–303, 1987.

Sharma, O., H. Upadhyaya, T. Braine-Bonnaire, and R. Sadourny, Experiments on regional forecasting using a streched-coordinate general circulation model, *J. Meteorol. Soc. Jpn.*, *16*, 263–271, 1987.

Szejwach, G., Determination of semi-transparent cirrus cloud temperature from infrared radiances: application to meteosat, *J. Appl. Meteorol.*, *21*, 384-393, 1982.

Tiedtke, M., A comprehensive mass flux

scheme for cumulus parametrization in large-scale models, *Mon. Weather. Rev.*, *117*, 1779–1800, 1989.

Xu, J., F. Qisong, Z. Xiang, and L. Jian, Cloud motion winds from fy-2 and GMS-5 meteorological satellites, in *Fourth International Winds Workshop, EUMETSAT Publ. EUM P 24*, pp. 52-57, Darmstadt, Germany, 1998.

M. Bonazzola, L. Picon, F. Hourdin, G. Sèze, and R. Sadourny, Laboratoire de Météorologie Dynamique du CNRS, 75252 Paris Cedex 05, France.

H. Laurent, Laboratoire d'étude des Transferts en Hydrologie et Environnement de l'Institut de Recherche pour le Développement, 75450 Paris, France.

H. Pawlowska, Institute of Geophysics, University of Warsaw, 02-093 Warsaw, Poland.

(Received January 14, 2000; revised October 4, 2000; accepted October 11, 2000.)